Adaptive photodetector for assisted Talbot effect

Article *in* Applied Optics · July 2008

DOI: 10.1364/AO.47.003778 · Source: PubMed

3 authors:

Ponciano Rodriguez-Montero
Instituto Nacional de Astrofísica, Óptica y Ele…
29 PUBLICATIONS **110** CITATIONS
SEE PROFILE

Cristina M Gómez-Sarabia
Universidad de Guanajuato
48 PUBLICATIONS **150** CITATIONS
SEE PROFILE

Jorge Ojeda-Castaneda
Universidad de Guanajuato
266 PUBLICATIONS **2,418** CITATIONS
SEE PROFILE

Adaptive photodetector for assisted Talbot effect

P. Rodríguez-Montero,[1,*] C. M. Gómez-Sarabia,[2] and J. Ojeda-Castañeda[2]

[1]National Institute for Astrophysics, Optics and Electronics, PB 216, Puebla 72000, Puebla, México

[2]University of Guanajuato, Campus Palo Blanco, Salamanca 36730, Guanajuato, México

*Corresponding author: ponciano@inaoep.mx

Received 5 March 2008; revised 17 June 2008; accepted 20 June 2008;
posted 20 June 2008 (Doc. ID 93500); published 11 July 2008

We use an adaptive photodetector for measuring the visibility of the Fresnel diffraction patterns generated by a grating. Visibility is measured in real time, with high spatial resolution, and without any signal processing. This method is well suited for analyzing the Talbot effect and its many applications. © 2008 Optical Society of America

OCIS codes: 070.6760, 040.0040, 190.5330, 120.1088, 100.2650.

1. Introduction

The Talbot effect has been used in interferometry [1,2] in a myriad of scientific and industrial applications. For example, Talbot interferometry is useful for ranging and for assessing displacements and position [3–5], for measuring the amplitude of vibration [6], for evaluating focal lengths [7–10], for testing collimation [11,12], for spectrometry [13,14], and for spatial filtering [15,16]. It is common to asses the visibility of the Talbot patterns by looking at the intensity distributions or by recording the Fresnel diffraction patterns with a CCD camera [17,18]. In both cases, we believe that the applications of the Talbot effect are hindered by the image acquisition technique.

On the other hand, we note that adaptive photodetectors based on the non-steady-state photoelectromotive force (pEMF) effect are useful for detecting small vibrations [19–21], for sensing laser-generated ultrasonic displacements [22], for characterizing femtosecond pulses [23], and for measuring the coherence length of several light sources [24].

Here, our aim is to use the pEMF effect for measuring the visibility of the Fresnel diffraction patterns of a binary grating. We show experimentally that visibility can be measured in real time, with high spatial resolution, and without any signal processing. Hence, photodetectors based on the pEMF are well suited for analyzing the Talbot effect.

For the sake of completeness, in Section 2, we briefly discuss the basics of adaptive photodetection. In Section 3, we describe the characterization procedures for setting up an adaptive photodetector. In Section 4, we report our visibility measurements of the Talbot effect. In Section 5, we summarize our contribution.

2. Adaptive Photodetection

In Fig. 1 we show the schematics of a typical setup for observing the pEMF effect. A vibrating interference pattern, $I(x,t)$, impinges on the surface of the photorefractive material, which is short-circuited. In this manner, passing through the material there is an alternating electrical current that is known as the pEMF signal. In this paper, the pEMF signal is denoted J^{Ω}.

It is common to describe the pEMF effect as follows [19,20]. Inside the photorefractive material, there is a relatively stable space charged electric field $E_{SC}(x)$, which is produced by conventional photorefractive recording. There is also a photoconductivity distribution that is proportional to the illuminating intensity distribution. In mathematical terms, $\sigma(x,t) \propto I(x,t)$. We assume that the photoconductive distribution follows the vibrations of the illuminating intensity distribution instantaneously. J^{Ω} is generated by the periodic modulation of the spatial shift between $E_{SC}(x)$ and $\sigma(x,t)$.

0003-6935/08/213778-06$15.00/0

A remarkable feature of the pEMF effect is its adaptive property. In other words, the photodetector can compensate for both slow phase shifts, in the interference pattern, and any wavefront distortion in the interfering beams [19].

In Fig. 1, θ denotes the angle between two interfering beams, and $\lambda = 633\,\text{nm}$ is the wavelength of the laser. We use the letters I_1 and I_2 to represent the intensities of beams 1 and 2, respectively. It is a common practice, in the photorefractive community, to use the expression

$$m = \frac{2\sqrt{I_1 I_2}}{(I_1 + I_2)} \tag{1}$$

for representing the contrast of two interfering beams. This definition is compatible with Michelson's definition of visibility; see Appendix A. In this paper, m refers to the visibility.

Because of the influence of the phase modulator, the interference pattern vibrates harmonically at angular frequency $\Omega = 2\pi f$. In [19,20], it is shown that if one does not apply any DC voltage to the photoconductive sample, then one can describe the variations of J^{Ω} as

$$J^{\Omega} = \left(\Delta\sigma_0 \pi \frac{k_B T}{e}\right) m^2 F(\nu) G(\Omega). \tag{2}$$

In Eq. (2), Δ is the amplitude of the phase modulation, σ_0 is the average photoconductivity of the photorefractive material, k_B is Boltzmann's constant, and T is the temperature. $F(\nu)$ denotes the spatial transfer function

$$F(\nu) = \frac{\nu}{1 + \nu^2 (2\pi L_D)^2}, \tag{3}$$

where ν is the spatial frequency of the interference pattern and L_D is the diffusion length of the photocarriers. Finally, we designate the temporal transfer function

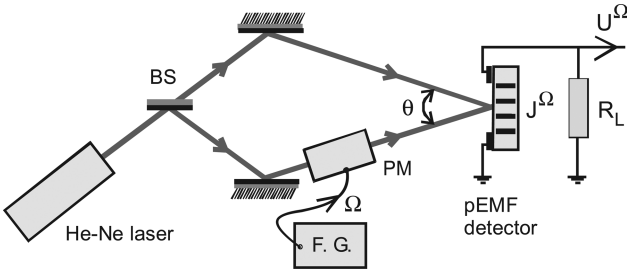

Fig. 1. Schematics of the optical setup for implementing the pEMF effect. We use the following notation. BS, beam splitter; F. G, function generator; PM, phase modulator; J^{Ω} is the pEMF current; and U^{Ω} is the voltage across the load resistor R_L.

$$G(\Omega) = \frac{-i\Omega/\Omega_0}{1 + i\Omega/\Omega_0} = \left\{\frac{\Omega/\Omega_0}{\left[1 + (\Omega/\Omega_0)^2\right]^{1/2}}\right\} \exp[i\varphi(\Omega)], \tag{4}$$

where the phase $\varphi(\Omega)$ is defined as

$$\tan[\varphi(\Omega)] = \Omega_0/\Omega. \tag{5}$$

Ω_0 is known as the dielectric cutoff frequency of the temporal transfer function $G(\Omega)$.

It is relevant here to note that Eq. (2) is obtained under the following assumptions: (a) only one type of photocarrier participates in the formation of the space charged electric field $E_{sc}(x)$; (b) the photocarriers have a short lifetime ($\tau \ll \Omega^{-1} \ll {\Omega_0}^{-1}$); (c) the interference pattern has low visibility ($m \ll 1$); and (d) the phase modulation has low amplitude ($\Delta \ll 1$ rad).

A remarkable property of Eq. (2) is that without any data processing, J^{Ω} is proportional to the square of the visibility, m^2. Next, we use this unique feature for directly measuring the visibility of the Fresnel diffraction patterns generated by a grating.

3. Adaptive Photodetector

For our adaptive photodetector, we use a piece of GaAs:Cr crystal with the dimensions 8 mm × 5 mm× 0.5 mm. The photorefractive material has a pair of silver electrodes at its front surface. The electrodes generate an effective interelectrode surface with the dimensions $L_X \approx 5\,\text{mm}$ and $L_y \approx 5\,\text{mm}$. Next, we attach the photorefractive material to a plastic substrate. Then, with a coaxial cable, we connect the silver electrodes to a lock-in amplifier.

As a first step of our characterization procedure, we measure J^{Ω} as a function of the visibility m, as is defined in Eq. (1). To this end, the adaptive photodetector is illuminated with a sinusoidal interference pattern. We keep constant the total intensity impinging onto the photodetector. However, we vary the relative intensity between the two interfering beams. Our experimental results are shown in Fig. 2. From this figure, in the interval (0.1, 0.85), we observe that J^{Ω} is linearly related to m^2, as is expressed in Eq. (2). Inside this interval, the linear relationship is expressed as the least-squares line

$$J^{\Omega} = 403m^2 - 9, \quad \text{with correlation coefficient } R = 0.99. \tag{6}$$

Of course, if one considers the data for the complete interval (0, 1), then the best fitting line is

$$J^{\Omega} = 423m^2 - 17, \quad \text{with } R = 0.99. \tag{7}$$

As a second step of our characterization procedure, we plot in Fig. 3 the experimental results of measuring J^{Ω} as a function of the spatial frequency, $\nu = 1/\Lambda = \sin\theta/\lambda$, of the interference pattern. This

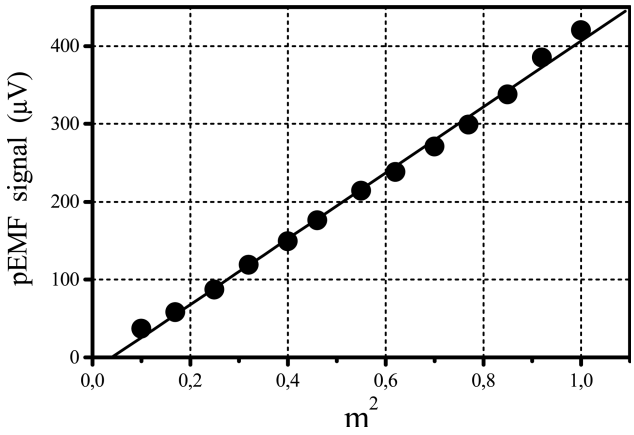

Fig. 2. Experimental results of J^{Ω} versus visibility of the interfering beams. The value of the average intensity is $I_0 \approx 3\,\mu\mathrm{W/mm^2}$. The modulation frequency is $f = 4\,\mathrm{KHz}$, the amplitude of the phase modulation is $\Delta \approx 300\,\mathrm{mrad}$, and the period of the interfering beams is $\Lambda \approx 100\,\mu\mathrm{m}$. The solid line is the best linear fit in the complete interval (0, 1).

result is particularly important when measuring J^{Ω} for any arbitrary interference patterns, which may be composed of several cosinusoidal components. The experimental curve shows a typical relationship for the pEMF effect; see [19,20]. We note that, in the log-log scale used in Fig. 3, the relationship can be approximated by two linear mappings relating J^{Ω} and ν. For the low-frequency region $\nu < 4000\,\mathrm{lines/m}$, J^{Ω} increases monotonically. For the high-spatial-frequency region, $\nu > 4000\,\mathrm{lines/m}$, J^{Ω} decreases monotonically. For spatial frequencies $\nu > 10,000\,\mathrm{lines/m}$, the least-squares line is

$$\log(J^{\Omega}) = 3.32 - 0.87\,\log(\nu) \quad \text{with correlation coefficient } R = 0.99 \tag{8a}$$

or, equivalently,

$$J^{\Omega} = 2090/\nu^{0.86}. \tag{8b}$$

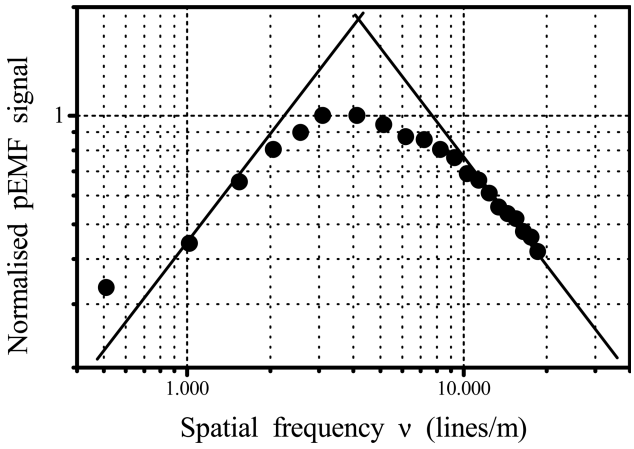

Fig. 3. Spatial transfer function: normalized values of J^{Ω} as a function of the spatial frequency, ν, of the interference pattern. Solid lines represent the approximated linear mappings.

As for the temporal transfer function of our photodetector, it behaves as predicted in Eq. (4), similar to the response of a high-pass filter. For an incident intensity of $3\,\mu\mathrm{W/mm^2}$ and a load resistor of $R_L = 20\,\mathrm{k\Omega}$, the dielectric cutoff frequency is $\Omega_0 \approx 3\,\mathrm{KHz}$. For the experiments reported here, we use as the load resistor R_L, the input resistance of the lock-in amplifier, with a nominal value of $100\,\mathrm{M\Omega}$.

4. Visibility Measurements

In Fig. 4, we show the schematics of our experimental setup for measuring the visibility of the Fresnel diffraction patterns (of a binary grating) by means of adaptive photodetectors. For the experimental setup, we use a He–Ne laser ($\lambda = 633\,\mathrm{nm}$). The laser beam has an initial power of 10 mW. We expand the laser beam by using a 20× microscope objective. As the spatial filter, we use a pinhole with a diameter that is equal to $10\,\mu\mathrm{m}$. For collimating the beam, we use a lens with a focal length that is equal to 200 mm. The lens diameter is equal to 25.4 mm.

For our experiments we select a binary grating with a fill factor that is equal to 0.5. To guarantee a decreasing relationship between J^{Ω} and ν, we select a binary grating with a nominal period $\Lambda_1 = 100\,\mu\mathrm{m}$, that is $\nu_1 = 10,000\,\mathrm{lines/m}$ Consequently, we can assume that the cosinusoidal components of the binary grating are inside the region where the pEMF signal (as a function of the spatial frequency) decays monotonically. See Fig. 3.

Next, we glue the grating to a low-frequency piezoelectric transducer. The piezoelectric induces the vibrations in the grating, as well as in the near-field, diffraction pattern. To fulfill the requirement of a small phase modulation Δ—as expressed in Eq. (2)—we set the piezoelectric transducer to produce vibrations that have amplitudes smaller than the wavelength of the laser radiation. We use a signal generator to drive the piezoelectric transducer. The same generator provides a reference signal for the lock-in amplifier.

Finally, we mount the adaptive photodetector on translational stage for scanning the visibility of the Talbot patterns along the optical axis, Z. The translational stage has a resolution of $10\,\mu\mathrm{m}$.

In Fig. 5 we show the experimental results, obtained by measuring J^{Ω}, as a function of the longitudinal displacements (optical axis) in steps of $250\,\mu\mathrm{m}\pm$

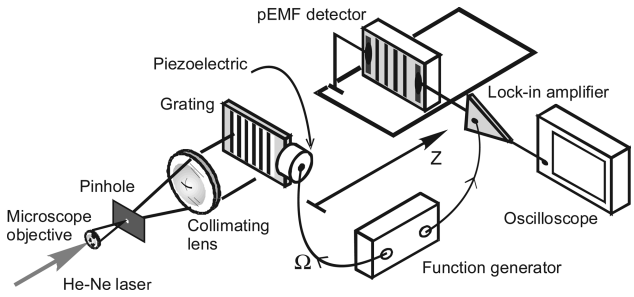

Fig. 4. Schematics of the optical setup for measuring the visibility of the self-images.

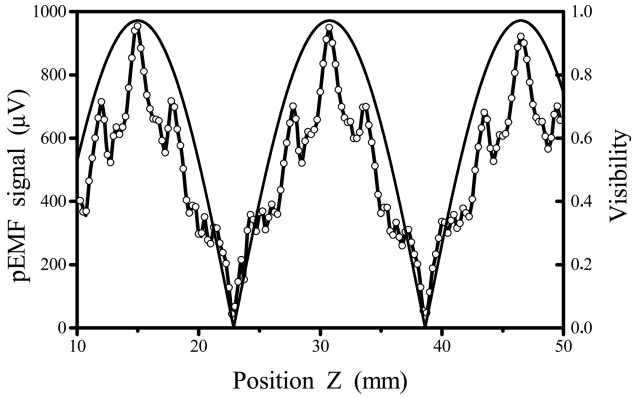

Fig. 5. Experimental results of J^{Ω} versus axial distance in steps of 250 μm. The visibility is measured between the fifth self-imaging plane and the sixth self-imaging plane. The reference signal is the theoretical visibility curve versus axial displacement.

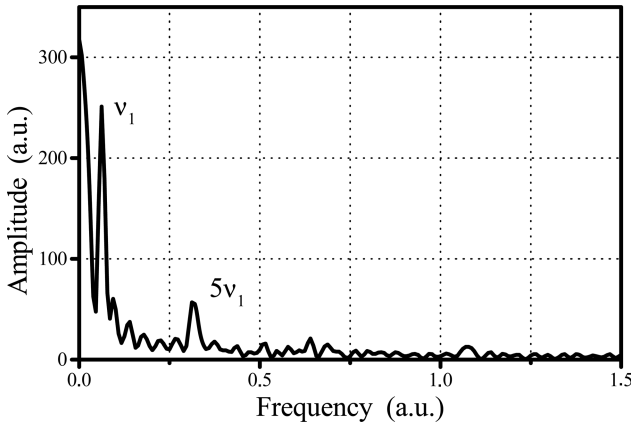

Fig. 6. Fourier spectrum of the visibility curve versus axial displacement, shown in Fig. 5.

5 μm. The frequency of modulation is $f = 600$ Hz. The time constant of the lock-in amplifier is 300 ms. The total intensity on the adaptive photodetector is $\approx 4\,\mu\mathrm{W/mm^2}$. Except by the integration time of the lock-in amplifier (which was set at 300 ms for these experiments) there is no electrical processing of the output signal. In Fig. 5, we show the raw data coming directly from the lock-in amplifier.

For gathering the data in Fig. 5, we place the adaptive photodetector between the self-image number 5 and the self-image number 6. From the experimental data, we are able to identify the axial positions of the self-images that have maximum visibility. In the middle of these self-images, we are able to identify the so-called negative self-images. That is, the Fresnel diffraction pattern of the grating is a self-image with reversed visibility. This type of Talbot images is associated with the use of a grating that has a fill factor that is equal to 0.5.

Furthermore, from the experimental data in Fig. 5, we are able to identify the plane where the Fresnel diffraction patterns have minimum visibility (uniform illumination). This plane is located at one quarter of the Talbot length. This result is also associated with the use of a Ronchi grating [25]. In the latter case, the values of J^{Ω} are close to the noise floor of our measuring system.

From Fig. 5, we note that our experimental results follow as a trend the theoretical visibility curve obtained in Appendix A. However, the experimental curve has some high-frequency components. For identifying the high-frequency components, we digitally evaluate the Fourier power spectrum of the visibility curve. As is depicted in Fig. 6, the Fourier power spectrum has a component $\nu = 5\nu_1$. We are unable to explain the presence of this high-frequency component.

To test the resolution capability of the adaptive photodetector, we perform the following test. We repeat the visibility measurements by placing the photodetector at axial steps of 50 μm $\pm$ 5 μm in an interval around the plane of minimum visibility. In Fig. 7, we show our experimental results.

From Fig. 7, we observe that the adaptive photodetector is capable of resolving points that are axially separated by 50 μm. The amplitude of J^{Ω} proved to be very stable. In fact, any fluctuations of J^{Ω} are inside the circles that we use in Figs. 5 and 7, for indicating the mean value of J^{Ω}. The uncertainty in the axial position ($\pm 5\,\mu$m) cannot be plotted in Figs. 5 and 7.

It is interesting that, by using the experimental data in Fig. 7, we find that the Talbot distance is $Z_T = (31.65 \pm 0.05)$ mm. This value is in good agreement with the theoretical prediction of $Z_T = 2\Lambda^2/\lambda = 31.60$ mm.

Finally, we comment on the speed of the measurements when an adaptive photodetector is used. According to [21], the operation speed is limited by the time that the photorefractive material takes to build up the space charge electric field $E_{\mathrm{SC}}(x)$. For adaptive photodetectors (that are based on GaAs crystals), this time is typically of the order of 10^{-7} s. For verifying the real-time acquisition capabilities, we substitute the manual translational stage by a motorized translational stage. Then, we visualize the measurements of J^{Ω} with a digital oscilloscope, which was connected to the output of the lock-in amplifier. In Fig. 8 we show a typical oscilloscope trace, which is obtained by measuring the

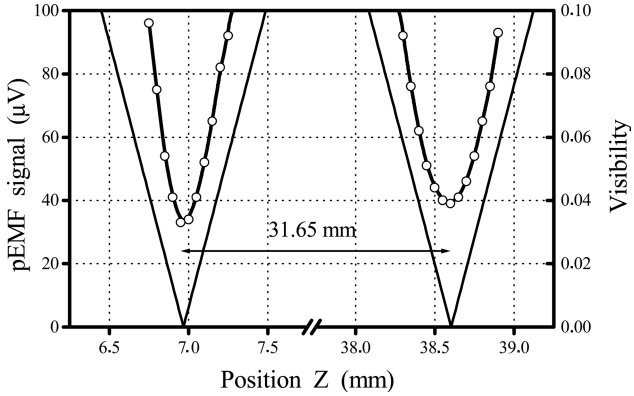

Fig. 7. Extended views of the signal variations in the neighborhood of zero visibility. Each experimental point is separated by 50 μm.

visibility as the motorized stage moves the detector along the Z axis. The range of longitudinal displacements in Fig. 8 is similar to the longitudinal range in Fig. 5. As is expected, the curve in Fig. 8 is similar to the curve in Fig. 5.

From Fig. 8, we note that our experimental results follow as a trend the theoretical visibility curve obtained in Appendix A. But again, the experimental curve has a high-frequency component at $\nu = 5\nu_1$. We are unable to explain this feature.

Preliminary experimental results lead us to conclude that the proposed adaptive photodetector is useful for measuring focal lengths and small vibrations that are on the millimeter scale. These applications are beyond our present scope.

5. Conclusions

The Fresnel diffraction (Talbot) patterns of a binary grating are useful for setting up low-cost and versatile devices for optical metrology. However, we believe that these devices are hindered by the experimental technique used for measuring the visibility of the Fresnel diffraction patterns. Hence, we have proposed to use adaptive photodetectors for measuring the visibility of the Talbot patterns. Adaptive photodetectors can produce an electrical current that is proportional to the square of the visibility of the Fresnel diffraction pattern.

Here, we have described the experimental steps for implementing an adaptive photodetector by using a GaAs:Cr photorefractive material. It proved to be a cheap, reliable, and very robust device.

We have measured the visibility of the Fresnel diffraction patterns, along the optical axis, in steps of 250 μm. Since we used a binary grating with a fill factor that is equal to one half, we were able to identify the so-called negative self-images as well as the planes where the Fresnel diffraction patterns have zero visibility.

The visibility curve (as a function of the displacements along the optical axis) exhibits the presence of a fifth-order harmonic, $\nu = 5\nu_1$, which we are unable to explain. This feature requires further study.

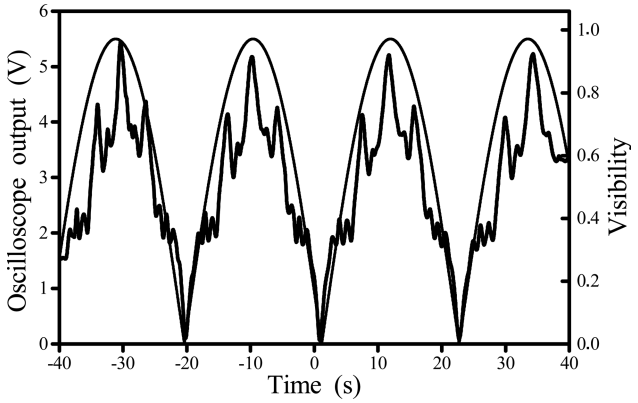

Fig. 8. Signal at the oscilloscope obtained when the adaptive photodetector is mounted in a motorized translation stage. The experimental conditions are similar to those in Fig. 5.

Finally, we have shown experimentally that the adaptive photodetector is capable of resolving points that are axially separated by 50 μm. Furthermore, we have verified experimentally that the adaptive photodetector can measure visibility in real time without the need of using any signal processing technique.

Therefore, the proposed technique is well suited for the metrological applications of the Talbot effect. In particular, the photodetecting technique may be useful for measuring focal lengths and for evaluating displacements in the millimeter range.

Appendix A

For describing the intensity distribution of the interference pattern of two beam beams, we denote the complex amplitude distribution (of any of the two possible beams) as

$$U_n(x) = \sqrt{I_n}\,\exp(i\varphi_n). \tag{A1}$$

Hence, the intensity distribution of the interference pattern is

$$I(x) = I_1 + I_2 + 2\sqrt{I_1 I_2}\,\cos(\varphi_2 - \varphi_1). \tag{A2}$$

Now, if one defines

$$I_{\max} = I_1 + I_2 + 2\sqrt{I_1 I_2}, I_{\min} = I_1 + I_2 - 2\sqrt{I_1 I_2}, \tag{A3}$$

then it is straightforward to show that Michelson's definition of visibility,

$$m = (I_{\max} - I_{\min})/(I_{\max} + I_{\min}) = 2\sqrt{I_1 I_2}/(I_1 + I_2). \tag{A4}$$

Equation (A4) is Eq. (1) in the main text. Next, we express as a Fourier series the complex amplitude transmittance, $T(x)$, of a binary grating, with fill factor that is equal to one half,

$$T(x) = \sum_{n=-\infty}^{\infty} C_n\,\exp(i2\pi x n/\Lambda). \tag{A5}$$

In Eq. (A5) the Fourier coefficients are

$$C_n = (1/2)\mathrm{sinc}(n/2). \tag{A6}$$

If the binary grating is approximated by three terms of its Fourier series, then

$$T(x) \approx (1/2) + (2/\pi)\cos(2\pi x/\Lambda). \tag{A7}$$

Hence, its Fresnel diffraction pattern can be expressed as follows:

$$U(x,z) \approx \frac{1}{2} + \frac{2}{\pi}\,\exp\left(\frac{-i\pi\lambda z}{\Lambda^2}\right)\cos\left(\frac{2\pi x}{\Lambda}\right). \tag{A8}$$

We obtain the intensity distribution by evaluating the square modulus of Eq. (A8), that is,

$$I(x,z) \approx \frac{1}{4} + \frac{2}{\pi}\cos\left(\frac{\pi\lambda z}{\Lambda^2}\right)\cos\left(\frac{2\pi x}{\Lambda}\right) + \left(\frac{4}{\pi^2}\right)\cos^2\left(\frac{2\pi x}{\Lambda}\right), \tag{A9}$$

or, equivalently,

$$I(x,z) \approx \frac{1}{4} + \frac{2}{\pi^2} + \frac{2}{\pi}\cos\left(\frac{\pi\lambda z}{\Lambda^2}\right)\cos\left(\frac{2\pi x}{\Lambda}\right) + \left(\frac{2}{\pi^2}\right)\cos\left(\frac{4\pi x}{\Lambda}\right). \tag{A10}$$

Next, we evaluate the maximum value and the minimum value of the intensity distribution,

$$I_{\max} = I(0,z) = \frac{1}{4} + \frac{2}{\pi^2} + \frac{2}{\pi}\cos\left(\frac{\pi\lambda z}{\Lambda^2}\right) + \left(\frac{2}{\pi^2}\right). \tag{A11}$$

$$I_{\min} = I\left(\frac{\Lambda}{2}, z\right) = \frac{1}{4} + \frac{2}{\pi^2} - \frac{2}{\pi}\cos\left(\frac{\pi\lambda z}{\Lambda^2}\right) + \frac{2}{\pi^2}. \tag{A12}$$

Then, according to the classical definition of visibility,

$$m = \lfloor 8\pi/(16+\pi^2)\rfloor \cos(\pi\lambda z/\Lambda^2). \tag{A13}$$

In Figs. 5 and 8 we plot the modulus of Eq. (A13)as a reference for making comparisons with our experimental results.

References

1. A. W. Lohmann and D. Silva, "An interferometer based on the Talbot effect," Opt. Commun. **2**, 413–415 (1971).
2. S. Yokozeki and T. Suzuki, "Shearing interferometer using the grating as the beam splitter," Appl. Opt. **10**, 1575–1580 (1971).
3. P. Chavel and T. C. Strand, "Range measurement using Talbot diffraction imaging of gratings," Appl. Opt. **23**, 862–871 (1984).
4. G. Schirripa Spagnolo, D. Ambrosini, and D. Paoleti, "Displacement measurement using the Talbot effect with a Ronchi grating," J. Opt. A Pure Appl. Opt. **4**, S376–S380 (2002).
5. C.-F. Kao and M.-H. Lu, "Optical encoder based on the fractional Talbot effect," Opt. Commun. **250**, 16–23 (2005).
6. Shashi Prakash, Sanjay Upadhyay, and Chandra Shakher, "Real time out-of-plane vibration measurement/monitoring using Talbot interferometry," Opt. Lasers Eng. **33**, 251–259 (2000).
7. S. A. Benton and D. P. Merrill, "Simplified Talbot interferometer for lens testing," Opt. Eng. **15**, 328–331 (1976).
8. Y. Nakano and K. Murata, "Talbot interferometry for measuring the focal length of a lens," Appl. Opt. **24**, 3162–3166 (1985).
9. P. Andrés, J. C. Barreiro, and J. Ojeda-Castaneda, "Focal length measuring technique using the Talbot effect," Proc. SPIE **0701**, 273–275 (1986).
10. M. Tebaldi, G. Forte, R. Torroba, N. Bolognini, and A. Tagliaferri, "Self-imaging pitch variation applied to focal length digital measurements," Opt. Commun. **250**, 10–15 (2005).
11. M. P. Kothiyal and R. S. Sirohi, "Improved collimation testing using Talbot interferometry," Appl. Opt. **26**, 4056–4057 (1987).
12. A. R. Ganesan and P. Venkateswarlu, "Laser beam collimation using Talbot interferometry," Appl. Opt. **32**, 2918–2920 (1993).
13. A. W. Lohmann, "A new Fourier spectrometer consisting of a two-gratings-interferometer," in *Proceedings of the Conference on Optical Instruments and Techniques*, K. J. Habell, ed. (Chapman and Hall, 1961), pp. 58–61.
14. H. L. Kung, A. Bhatnagar, and D. A. B. Miller, "Transform spectrometer based on measuring the periodicity of Talbot self-images," Opt. Lett. **26**, 1645–1647 (2001).
15. J. Ojeda-Castañeda and E. E. Sicre, "Tunable bandstop filter for binary objects: a self-imaging technique," Opt. Commun. **47**, 183–186 (1983).
16. A. W. Lohmann, J. Ojeda-Castañeda, and E. E. Sicre, "Multiple interaction bandstop filters based on the Talbot effect," Opt. Commun. **49**, 388–392 (1984).
17. M. Takeda, H. Ina, and S. Kobayashi, "Fourier-transform method of fringe-pattern analysis for computer-based topography and interferometry," J. Opt. Soc. Am. **72**, 156–160 (1981).
18. R. Torroba, N. Bolognini, M. Tebaldi, and A. Tagliaferri, "Positioning method based on digital Moiré," Opt. Commun. **209**, 1–6 (2002).
19. S. Stepanov, "Photo-electromotive force in semiconductors," in *Handbook of Avanced Electronic and Photonics Materials and Devices*, H. S. Nalwa, ed. (Academic, 2001), Vol. 2, pp. 205–272.
20. M. P. Petrov, I. A. Sokolov, S. I. Stepanov, and G. S. Trofimov, "Non-steady-state photo-electromotive force induced by dynamic gratings in partially compensated photoconductors," J. Appl. Phys. **68**, 2216–2225 (1990).
21. N. Korneev, S. Mansurova, P. Rodríguez, and S. Stepanov, "Fast and slow processes in the dynamics of near-surface charge grating formation in GaAs," J. Opt. Soc. Am. B **14**, 396–399 (1997).
22. S. Stepanov, P. Rodriguez, S. Trivedi, and C. C. Wang, "Effective broadband detection of nanometer laser-induced ultrasonic surface displacements by CdTe:V adaptive photoelectromotive force detector," Appl. Phys. Lett. **84**, 446–448 (2004).
23. Y. Ding, I. Lahiri, D. Nolte, G. J. Dunning, and D. M. Pepper, "Electric-field correlation of femtosecond pulses by use of a photoelectromotive force detector," J. Opt. Soc. Am. B **15**, 2013–2017 (1998).
24. M. L. Arroyo-Carrasco, P. Rodriguez-Montero, and S. Stepanov, "Measurement of the coherence length of diffusely scattered laser beams with adaptive photodetectors," Opt. Commun. **157**, 105–110 (1998).
25. J. Ibarra and J. Ojeda-Castaneda, "Talbot interferometry: a new geometry," Opt. Commun. **96**, 294–301 (1993).